*Article*

# Dealloying-Derived Nanoporous Cu$_6$Sn$_5$ Alloy as Stable Anode Materials for Lithium-Ion Batteries

**Chi Zhang \*, Zheng Wang, Yu Cui, Xuyao Niu, Mei Chen, Ping Liang, Junhao Liu, Runjun Liu, Jingcong Li and Xin He \***

School of Applied Physics and Materials, Wuyi University, Jiangmen 529020, China; wangzh1104@163.com (Z.W.); CuiYu2468@163.com (Y.C.); nxy13007149948@163.com (X.N.); chenmei116@126.com (M.C.); ping_liang@126.com (P.L.); wyuljh@163.com (J.L.); lrj3118004629@163.com (R.L.); lijingcong1026@163.com (J.L.)
\* Correspondence: chizhang@wyu.edu.cn (C.Z.); hexinwyu@126.com (X.H.)

**Abstract:** The volume expansion during Li ion insertion/extraction remains an obstacle for the application of Sn-based anode in lithium ion-batteries. Herein, the nanoporous (np) Cu$_6$Sn$_5$ alloy and Cu$_6$Sn$_5$/Sn composite were applied as a lithium-ion battery anode. The as-dealloyed np-Cu$_6$Sn$_5$ has an ultrafine ligament size of 40 nm and a high BET-specific area of 15.9 m$^2$ g$^{-1}$. The anode shows an initial discharge capacity as high as 1200 mA h g$^{-1}$, and it remains a capacity of higher than 600 mA h g$^{-1}$ for the initial five cycles at 0.1 A g$^{-1}$. After 100 cycles, the anode maintains a stable capacity higher than 200 mA h g$^{-1}$ for at least 350 cycles, with outstanding Coulombic efficiency. The ex situ XRD patterns reveal the reverse phase transformation between Cu$_6$Sn$_5$ and Li$_2$CuSn. The Cu$_6$Sn$_5$/Sn composite presents a similar cycling performance with a slightly inferior rate performance compared to np-Cu$_6$Sn$_5$. The study demonstrates that dealloyed nanoporous Cu$_6$Sn$_5$ alloy could be a promising candidate for lithium-ion batteries.

**Keywords:** dealloying; nanoporous; Cu6Sn5 alloy; lithium-ion battery

## 1. Introduction

The development of portable electronic devices urgently requires lithium-ion batteries (LIBs) with a high capacity and long lifespan [1–3]. Currently, extensive efforts have been devoted to developing alternative anode materials, e.g., metal oxide, alloys and group IVA elements, to boost the capacity of LIBs [1,4,5]. Micro-pillar splitting and micro-cantilever bending have been proposed to evaluate the mechanical behaviors of materials at the micro-scale, and micro-pillar splitting is commonly employed to analyze the fracture toughness of battery electrode materials and solid state electrolyte [6]. Tin (Sn) is regarded as one of the promising anode substitutes due to its high theoretical gravimetric capacity (994 mA h g$^{-1}$ for Li$_{22}$Sn$_5$), low cost, great safety and low working potential window (0.3–0.6 V) [7–9]. However, Sn suffers from violent irreversible capacity loss and disintegration due to its Li-driven volume expansion (up to 259%) during lithiation and de-lithiation cycling, which impedes its application in commercial LIBs [7,10].

Several approaches have been proposed to overcome the volume expansion issue. One is to reduce the size of the Sn-based materials, i.e., construction of nanostructures. For instance, a 3D nanocomposite consisted of 3D structured Sn scaffold and a hollow Sn sphere was fabricated as the LIBs anode [11]. The anode exhibited a capacity of 1700 mA h cm$^{-3}$ for over 200 cycles at 0.5 C. The high cycling stability could be attributed to the 3D nanostructured design that accommodated the volume expansion during charge/discharge [11]. Another effective approach is to construct Sn/carbon or Sn/metal composite, in which the carbon substrate or metal can act as the buffer to bear the volume change of Sn. Wang's group designed a mesoporous carbon/Sn anode for Li-ion and Na-ion batteries, in which the mesoporous carbon was proposed to accommodate the volume change of Sn nanoparticles during ion insertion and extraction [12]. A Sn/graphite anode presented improved

capacity retention with only 0.7% loss per cycle [13]. Nanocable-like Sn-core/carbon-sheath anode materials have been fabricated by chemical vapor deposition, delivering a specific capacity of 630 mA h g$^{-1}$ after 100 cycles at a current density of 100 mA g$^{-1}$ [14]. In addition, graphene-confined Sn nanosheets and 3D hierarchical $SnO_2$/graphene frameworks were designed, showing enhanced lithium storage capability [15,16]. Liu et al. reported a 3D nanocomposite including both a 3D structured Sn scaffold and a hollow Sn sphere within each cavity where all the free Sn surfaces are coated with carbon, showing a high volumetric capacity of $\sim$1700 mA h cm$^{-3}$ over 200 cycles at 0.5 C, and a capacity greater than 1200 mA h cm$^{-3}$ at 10 C [11]. Combining Sn with metals could form intermetallic compounds and the metal could also act as the buffer to accommodate the volume expansion [1,17]. A $Ni_3Sn_2$ microcage showed stable capacity of 534 mA h g$^{-1}$ after 1000 cycles at the current density of 1 C [17]. Single-crystalline $FeSn_2$ nanospheres with uniform small particle size have been synthesized, showing better electrochemical performances than other nano-spherical intermetallic compounds such as $Cu_6Sn_5$, $CoSn_3$ and $Ni_3Sn_4$, due to its crystal structure [18]. In addition, Sn-Co alloy nanoparticles encapsulated in a porous 3D graphene network was also applied as the LIB anode [19].

In addition to the above-mentioned materials, the most studied Sn-based materials are Cu-Sn alloys, as copper owns high conductivity and elasticity, and $Cu_6Sn_5$ possesses the high theoretical capacity of 605 mA h g$^{-1}$ [20–25]. Several approaches have been applied to fabricate $Cu_6Sn_5$ nanoparticles, film, or nanowires [20,26–29]. A solution route was used to synthesize dendrite $Cu_6Sn_5$ powers [27]. A facile one-step electrodepositing method could also form $Cu_6Sn_5$ alloy on the Cu foil, and the alloy electrode showed a discharge capacity of 462 mA h g$^{-1}$ [30]. A core-shell Cu@$Cu_6Sn_5$ nanowire was synthesized via an electrodeposition process, and the anode showed excellent rate performance even at high current density of 20 C [31]. Recently, dealloying, a powerful method to fabricate nanoporous metals, was applied to fabricate $Cu_6Sn_5$ nanostructure for fabrication LIB anode [22,25,28]. Liu et al. dealloyed $Cu_{17}Sn_7Al_{76}$ alloy in a 1 M NaOH to obtain a 3D nanoporous Cu-Sn electrode. The electrode presents a capacity of 566 mA h g$^{-1}$ at a current density of 1670 mA g$^{-1}$ [25]. The study found that the nanopores facilitated the penetration of Li$^+$ ions. A nanoporous $Cu_6Sn_5$/Cu composite was generated via a similar method by dealloying $Al_{10}Cu_3Sn$ alloy [22,32]. The hierarchical porous structure promoted the mass transport and accommodated the volume change; thus, the as-dealloyed composite displayed enhanced stability and rate performance [22].

In our previous report, we found that by changing Cu and Sn ratio in the Mg-Cu-Sn alloy, Cu-Sn alloys or composite with different phase compositions can be achieved via dealloying [28]. Herein, in this study, we applied the as-dealloyed $Cu_6Sn_5$ alloy and $Cu_6Sn_5$/Sn composite as the LIB anode. The as-dealloyed anode was found to have excellent cycling stability and rate performance due to the nanoporous structure. Moreover, the anode material has good thermal stability due to the formation of intermetallic $Cu_6Sn_5$, favoring the cycling. The ex situ XRD proved the reverse phase transformation between $Cu_6Sn_5$ and $Li_2CuSn$ during charge/discharge process.

## 2. Experimental

### 2.1. Synthesis of Nanoporous Cu₆Sn₅ Alloy and Cu₆Sn₅/Sn Composite

$Mg_{67}Cu_{18}Sn_{15}$ and $Mg_{66}Cu_{10.2}Sn_{23.8}$ (at.%) precursor ribbons were prepared from rapid solidification. Pure Mg, Cu and Sn metal blocks (purity: 99.9 wt.%) were melted in an alumina crucible using a resistance furnace (KYKY Technology Co., Ltd., Shenyang, China) under the protection of covering agent at about 800 °C. The melt liquid was cast into an alloy rod in a module. The obtained alloy rod was cut into ingots and remelted at 800 °C using a high-frequency induction furnace (KYKY Technology Co., Ltd., Shenyang, China) in a quartz tube with a pinhole below. The alloy melt was blasted onto a copper roller spinning at 1000 revolutions per minute from the pinhole by an Ar blow. The precursor ribbons obtained were collected for dealloying. The dealloying of Mg-Cu-Sn precursor ribbons was performed in a 1 wt.% tartaric acid (TA) at room temperature until no bubbles

emerged. The as-dealloyed ribbons were rinsed with deionized water and dehydrated alcohol for further characterizations and applications.

### 2.2. Microstructural Characterization

The microstructures of the as-dealloyed samples were investigated with scanning electron microscope (SEM, LEO 1530P, LEO Electron Microscopy Ltd., Oberkochen, Germany) and transmission electron microscope (TEM, Philips CM 20, FEI Company, Hillsboro, OR, USA). The crystalline nature was probed using high-resolution TEM (HRTEM, FEI Tecnai G2, Thermo Fisher Scientific Inc., Waltham, MA, USA) and selected-area electron diffraction (SAED, FEI Tecnai G2, Thermo Fisher Scientific Inc., Waltham, MA, USA). Nitrogen adsorption/desorption isotherms were measured with a surface area and porosity analyzer (Gold APP V-Sorb 2800, Gold APP Instruments, Beijing, China) at 77 K. Specific surface area was determined using the Brunauer–Emmett–Teller (BET) method. Pore size distribution was calculated from the adsorption branch by the Barrett–Joyner–Halenda (BJH) method using the corrected form of Kelvin equation. The ex situ XRD patterns of the discharged/charged samples were determined by a XD-3 diffractometer (Beijing Purkinje, Beijing Purkinje General Instrument Co., Ltd., Beijing, China) equipped with Cu-Ka radiation as described before [33,34]. The batteries were cycled to the required voltage and then opened for the ex situ XRD testing. A dimethyl carbonate (DMC) solution was used to remove the lithium salt of the cycled electrodes before testing.

### 2.3. Electrochemical Measurement

The as-dealloyed samples were ball-milled to fine powders with zirconia beads at a rotation speed of 300 rpm for 3 h. The $Cu_6Sn_5$ or $Cu_6Sn_5$/Sn powders (80 wt.%) were ground with acetylene black (Super-P, 10 wt.%) and polyvinylidene fluoride (PVDF) binder (10 wt.%) in N-methyl-2-pyrrolidinone (NMP) solvent to make a slurry. The slurry was coated onto Cu foil and further dried at 80 °C for 12 h under vacuum. The coated Cu foil was punched into disk shape of 12 mm in diameter, with the low mass loading of around 0.5 mg/cm$^2$. The as-prepared foil was used as the working electrode. A Li foil was used as both the reference electrode and counter electrode and a polypropylene (PP) film (Celgard 2325) was utilized as the separator. The electrolyte was made by mixing 1.0 M LiPF$_6$ with ethylene carbonate (EC) and DMC (1:1 by volume). The CR2032-type coin cells were assembled in an argon-filled glove box (Mikrouna Co. Ltd., Shanghai, China), with oxygen and moisture levels below 0.1 ppm. The galvanostatic discharging/charging tests were conducted at various current densities at the voltage window between 0.01 and 2.00 V (vs. Li$^+$/Li) using a LANDCT2001A test system. Cyclic voltammetry (CV) was conducted at a scan rate of 0.1 mV s$^{-1}$ between 0.01 and 2.00 V (vs. Li$^+$/Li) on an electrochemical workstation (CHI 660E).

### 3. Results and Discussions

The phase compositions of the precursors and dealloyed samples were confirmed by XRD in Figure 1. As exhibited in our previously reported study [28], the starting precursors $Mg_{67}Cu_{18}Sn_{15}$ (Figure 1a) and $Mg_{66}Cu_{10.2}Sn_{23.8}$ (Figure 1b) both consist of $Mg_2Sn$ (PDF # 65-2997) and $Mg_2Cu$ (PDF # 65-5460) phases. Only a minor amount of $Mg_2Cu$ is present, which indicates that substantial Cu enters the lattice of $Mg_2Sn$ to form $Mg_2(Sn,Cu)$ phase. The dealloying of $Mg_{67}Cu_{18}Sn_{15}$ (Figure 1c) and $Mg_{66}Cu_{10.2}Sn_{23.8}$ (Figure 1d) in 1 wt.% TA resulted in the formation of np-$Cu_6Sn_5$ (PDF # 65-2303) alloy and $Cu_6Sn_5$/Sn (PDF # 65-2303/PDF # 65-0296) composites, respectively, as described in ref [28]. It has been discussed that the formation of $Cu_6Sn_5$ involved the selective dissolution of Mg and co-diffusion of Cu and Sn [28]. The phase formation process was different from the dealloying of Al-Cu-Sn alloys, of which heating was required to form Cu-Sn alloys [22,35]. The difference in precursor type not only determines the dealloying process, but also has an effect on the microstructure of dealloyed alloys. As shown in Figure 2a and Figure S1, the as-dealloyed $Cu_6Sn_5$ derived from $Mg_{67}Cu_{18}Sn_{15}$ has ultra-fine

bi-continuous ligament-channel morphology. EDS spectra confirms the co-existence of Cu and Sn (Figure 2b). Magnified TEM image shows that the average pore size is below 40 nm (Figure 3a), which is comparable to that from dealloying of $Al_{10}Cu_3Sn$ in a 20 wt.% NaOH solution [22]. When increasing the content of Sn to 23.8 at.%, large skeletons with particles attached instead of nanoporous ligament-channel structure was formed (Figure 2c or Figure 3b and Figure S1). Combined with XRD results in ref [28], the skeletons should be $Cu_6Sn_5$ while the particles are composed of Sn. EDS spectra in Figure 2d shows higher relative Sn contents in the composite, corresponding to higher Sn ratio in the precursor. HRTEM in Figure 3c shows well-aligned lattices corresponding to as-dealloyed $Cu_6Sn_5$ alloy. The lattice distance indicates that the ligaments are identified to $Cu_6Sn_5$. Moreover, the corresponding FFT pattern (inset of Figure 3c) verifies the nanocrystalline nature of $Cu_6Sn_5$ ligaments. Figure 3d,e exhibit the HRTEM images and corresponding FFT patterns of as-dealloyed $Mg_{66}Cu_{10.2}Sn_{23.8}$ precursor. The spacing distances of lattice fringes corresponds to the (021) crystal plane (0.34 nm) of $Cu_6Sn_5$ (Figure 3d) and (101) plane (0.28 nm) of Sn (Figure 3e), respectively.
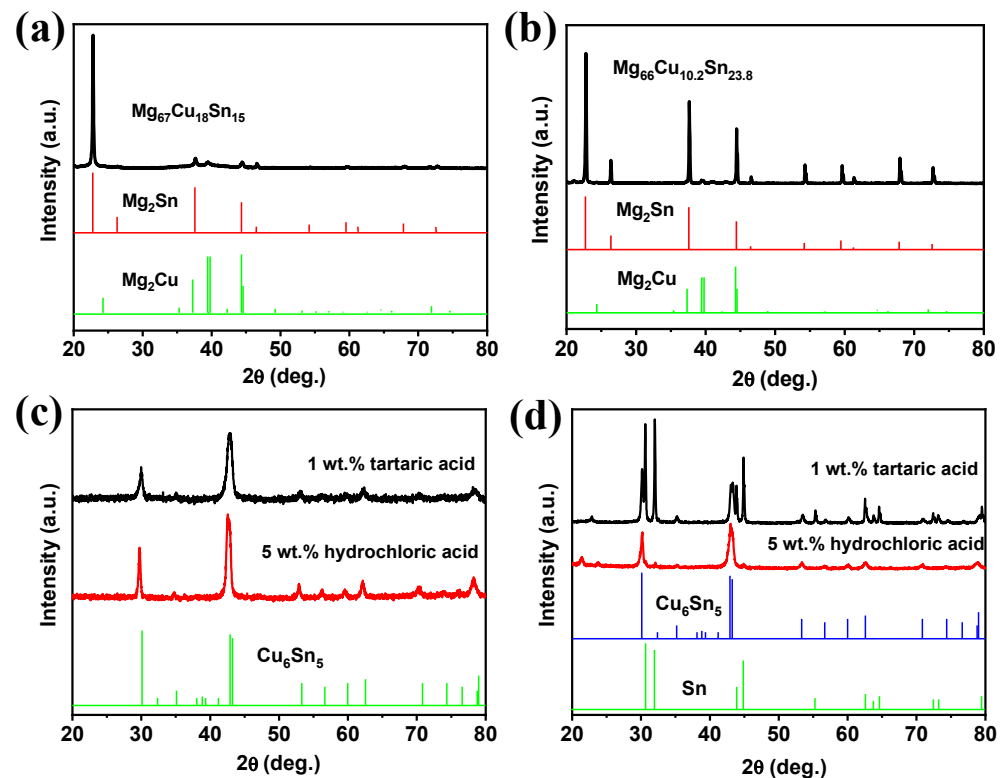


**Figure 1.** XRD patterns of (**a**) $Mg_{67}Cu_{18}Sn_{15}$ and (**b**) $Mg_{66}Cu_{10.2}Sn_{23.8}$ precursors; (**c**) dealloyed $Cu_6Sn_5$ and (**d**) dealloyed $Cu_6Sn_5/Sn$ composite. Reproduced from Ref. [28] with permission from the Royal Society of Chemistry.

The specific surface areas and pore distributions of as-dealloyed np-$Cu_6Sn_5$ are determined by $N_2$ adsorption-desorption method. Figure 4a presents the $N_2$ adsorption–desorption isotherms, which corresponds well to the type IV curve with a H3 hysteresis loop, indicating the formation of mesoporosity [36]. The BET-specific surface area is calculated as 15.9 $m^2 g^{-1}$, which is comparable to np-$Cu_6Sn_5/Cu$ composite from the dealloying of $Al_{10}Cu_3Sn$ [22]. The pore size distribution derived from the adsorption branch of the isotherm using the BJH model. The result (Figure 4b) shows that the pore size distributes in the range of 10–40 nm, in accordance with the TEM observation. The relatively high specific surface areas and robust ligament-channel structure might facilitate the diffusion of Li ions and alleviate the volume expansion during the charge/discharge process.
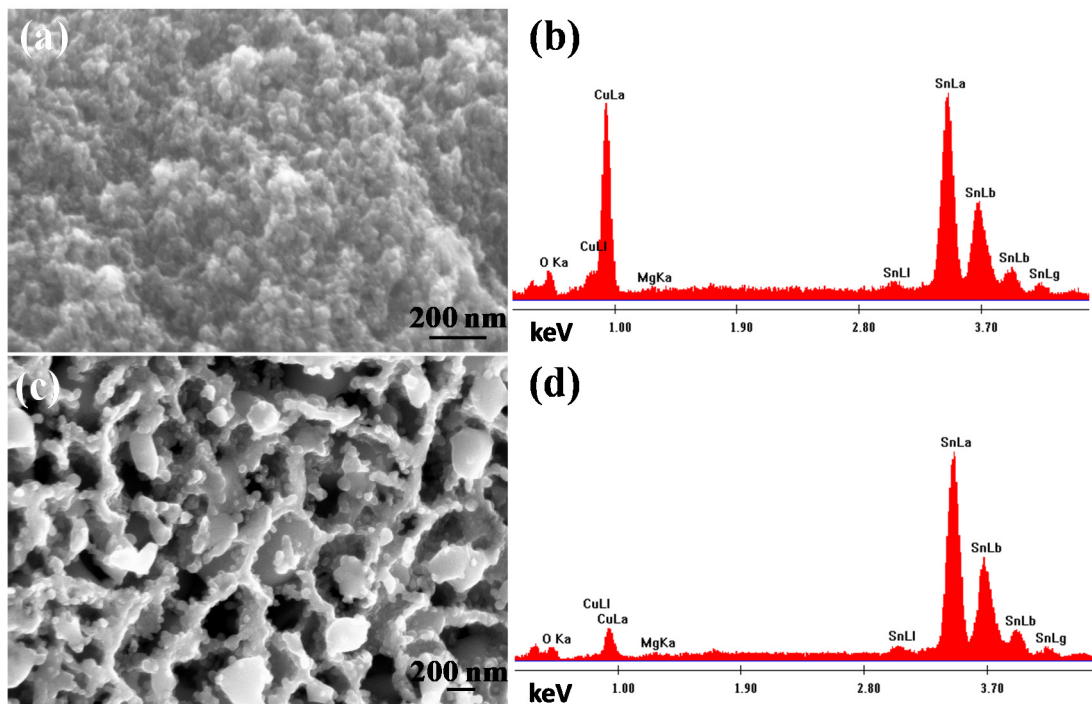
**Figure 2.** The SEM images and corresponding EDS spectra of (**a**,**b**) $Mg_{67}Cu_{18}Sn_{15}$ and (**c**,**d**) $Mg_{66}Cu_{10.2}Sn_{23.8}$ after dealloying in 1 wt.% TA.
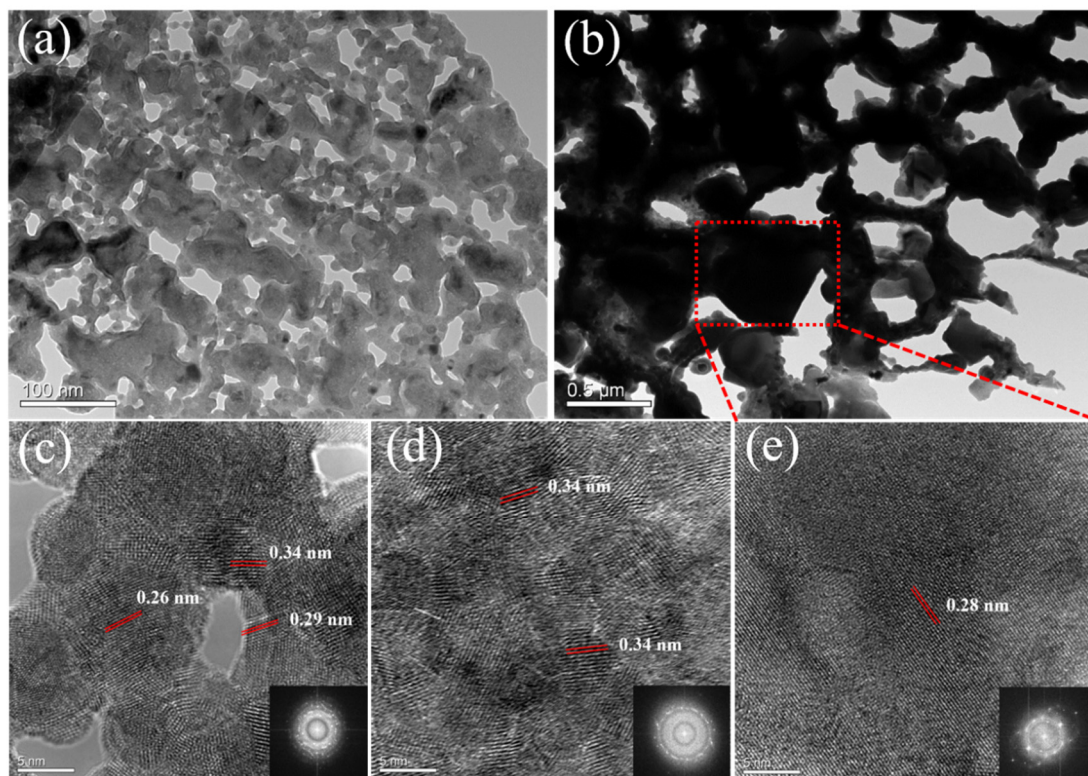


**Figure 3.** TEM images of dealloyed (**a**) $Mg_{67}Cu_{18}Sn_{15}$ and (**b**) $Mg_{66}Cu_{10.2}Sn_{23.8}$; HRTEM of dealloyed (**c**) $Mg_{67}Cu_{18}Sn_{15}$, (**d**) ligament domain and (**e**) particle domain of $Mg_{66}Cu_{10.2}Sn_{23.8}$. Insets of (**c**–**e**) are the corresponding FFT patterns.
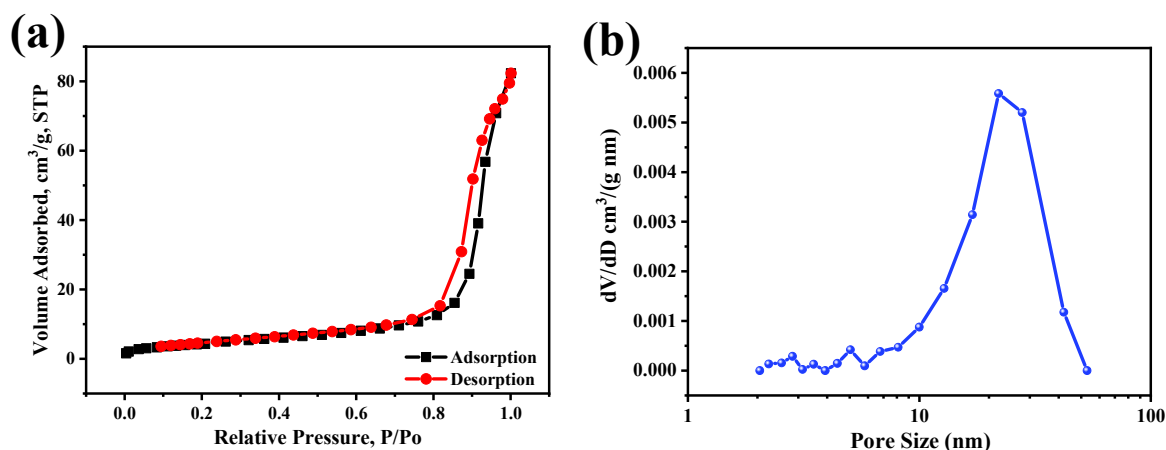
**Figure 4.** (**a**) $N_2$ adsorption/desorption isotherms of the as-dealloyed nanoporous $Cu_6Sn_5$. (**b**) The pore size distribution.

CVs at a scan rate of 0.1 mV s$^{-1}$ between 0.01 and 2.5 V (vs. Li$^+$/Li) are shown in Figure 5a. In the first cathodic process, np-$Cu_6Sn_5$ anode shows a peak at 0.77 V (vs. Li$^+$/Li), due to the irreversible reactions in the initial cycle [22]. The irreversible reactions might be attributed to the formation of solid-electrolyte interface (SEI). The CV peaks start to overlap from the second cycle, indicating that the anode becomes stable after the first cycle (Figure 5a). The performance of as-dealloyed $Cu_6Sn_5$ anode was evaluated using galvanostatic discharge–charge cycling. Figure 5b exhibits the initial five charge/discharge curves between 0.01 V (vs. Li$^+$/Li) and 2.0 V (vs. Li$^+$/Li) of the dealloyed $Cu_6Sn_5$ anode at the current density of 0.1 A g$^{-1}$. For the first cycle, the discharge process shows a plateau at around 0.25 and 0.77 V (vs. Li$^+$/Li), corresponding to the CV curve in Figure 5a. The discharge processes from the second cycle show obvious potential plateau at around 0.3 V (vs. Li$^+$/Li), in correspondence with the slight anodic peak from CV curves. The charge processes have plateaus at around 0.5 and 0.75 V (vs. Li$^+$/Li), which were also found in other $Cu_6Sn_5$-based materials [21–24,26]. To further study the phase transition during the charge/discharge process, the ex situ XRD analysis was performed. The pristine np-$Cu_6Sn_5$ clearly shows the peaks indexed to $Cu_6Sn_5$ phase (PDF # 65-2303) (Figure 5c). After fully discharging to 0 V for the first cycle, $Cu_6Sn_5$ phase disappears, and $Li_2CuSn$ phase (PDF # 65-5125) emerges at around 24.5 °C and 40.6 °C. The XRD pattern corresponding to the fully charged state of the second cycle confirms the transition from $Li_2CuSn$ to $Cu_6Sn_5$ again. Furthermore, the second fully discharged process proves the reversible conversion from $Cu_6Sn_5$ to $Li_2CuSn$. The ex situ XRD patterns indicate the reversible conversion of $Cu_6Sn_5$ to $Li_2CuSn$ during the charge/discharge process. Figure 5d shows the cycling performance of np-$Cu_6Sn_5$ alloy at the current density of 0.1 A g$^{-1}$. The initial discharge capacity is as high as 700 mA h g$^{-1}$, slightly higher than that from electrodeposited $Cu_6Sn_5$ alloy film [26]. The higher capacity could be attributed to the nanoporous ligament-channel structure that facilities the diffusion of electrolyte and the reduced Li-ions insertion pathway into the $Cu_6Sn_5$ ligaments [8,9]. The capacity can be maintained higher than 500 mA h g$^{-1}$ for at least 20 cycles and keep at ~200 mA h g$^{-1}$ for the following 400 cycles with the Coulombic efficiency of nearly 100%. The residual stress of electrodes is related to the performance and stability of energy generation devices such as LIBs here, and np-$Cu_6Sn_5$ with bi-continuous ligament-channel structure own strain relaxation, favoring the cyclability of LIBs [37]. The decay of capacity is induced by the alloy aggregation and collapse of porous structure during cycling, and the stability of np-$Cu_6Sn_5$ anode is expected to be improved by adjusting the constituent of alloy precursors and dealloying conditions in the future. The np-$Cu_6Sn_5$ anode also presents excellent rate performance, as illustrated in Figure 5e,f. At the current density of 0.1 A g$^{-1}$, the capacity is ~900 mA h g$^{-1}$ for the first cycle and maintains at higher than 700 mA h g$^{-1}$ for 10 cycles. With the current density increasing to 2.0 A g$^{-1}$, the capacity gradually decreases to ~380 mA h g$^{-1}$. The anode recovers to a capacity of around 600 mA h g$^{-1}$ when the current density is reversed to 0.1 A g$^{-1}$. The

results demonstrate that the nanoporous structure gives an excellent rate performance to the $Cu_6Sn_5$ anode, even after experiencing the high current density of 2.0 A $g^{-1}$. The anode was also performed under 0.5 A $g^{-1}$ to investigate its possible application under a higher current density. As shown in Figure S2, after 100 cycles, the anode can maintain its capacity higher than 150 mA h $g^{-1}$ for at least 1000 cycles, demonstrating excellent stability.
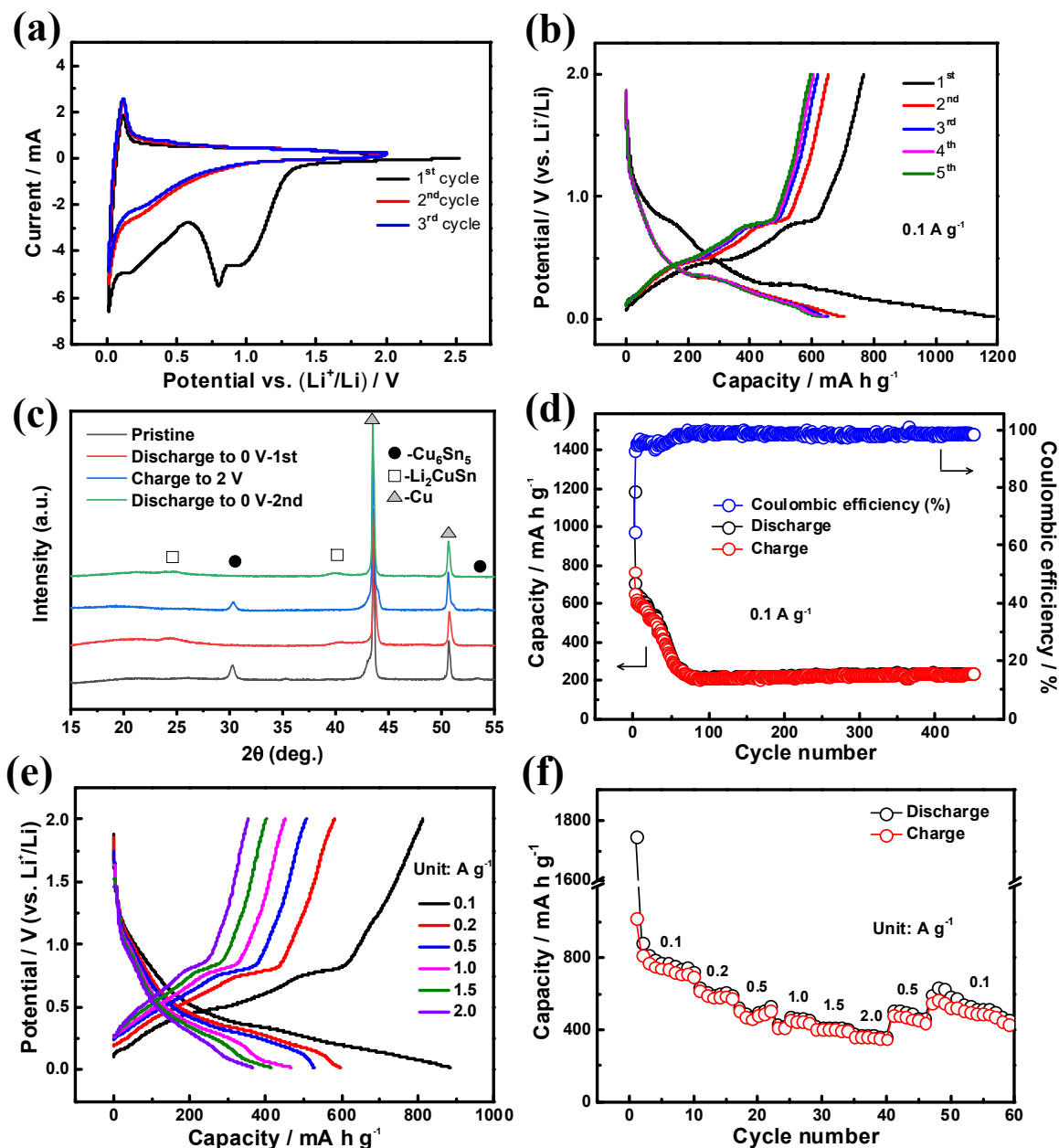


**Figure 5.** (**a**) CVs at a scan rate of 0.1 mV s$^{-1}$ between 0.01 and 2.5 V (vs. Li$^+$/Li). (**b**) The initial five charge/discharge profiles of as-dealloyed $Cu_6Sn_5$ anode with the current density of 0.1 A g$^{-1}$. (**c**) Ex situ XRD patterns collected at various states. (**d**) Cycling performance of the $Cu_6Sn_5$ at current density of 0.1 A g$^{-1}$. (**e**) The charge–discharge voltage profiles of the $Cu_6Sn_5$ alloy electrode at various current densities from 0. 1 A g$^{-1}$ to 2.0 A g$^{-1}$. (**f**) Rate performance at various current densities from 0. 1 A g$^{-1}$ to 2.0 A g$^{-1}$.

The charge/discharge cycling performance of $Cu_6Sn_5$/Sn composite was also tested. The initial charge capacity is higher than 800 mA h g$^{-1}$, better than that of $Cu_6Sn_5$, suggesting the contribution of Sn in the composite (Figure 6a). The capacity can be kept at around 200 mA h g$^{-1}$ for at least 550 cycles, comparable to that of np-$Cu_6Sn_5$. At a higher current density of 0.5 A g$^{-1}$, the capacity could maintain 150 mA h g$^{-1}$ (Figure S3). The $Cu_6Sn_5$/Sn

composite also shows an inferior rate performance, as shown in Figure 6b. When the current density was reversed to 0.2 A g$^{-1}$, the capacity could only maintain around 60% of its initial capacity at 0.2 A g$^{-1}$. The inferior cycling performance might be attribute to the Sn particles with large volume expansion during charge/discharge process [1].
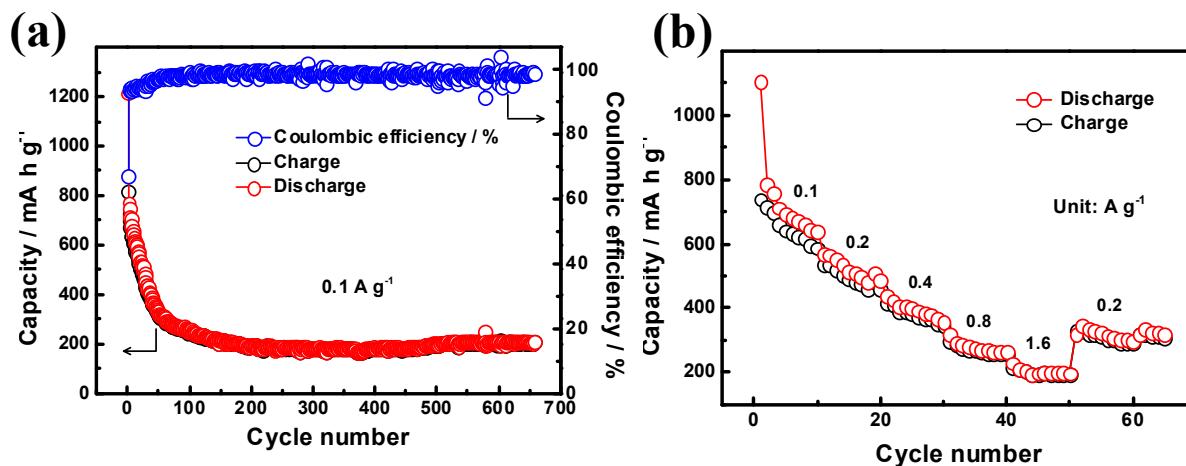


**Figure 6.** (**a**) Cycling performance of the Cu$_{16.2}$Sn$_{23.8}$ at current density of 0.1 A g$^{-1}$. (**b**) Rate performance at various current densities from 0. 1 A g$^{-1}$ to 1.6 A g$^{-1}$.

## 4. Conclusions

In summary, nanoporous Cu$_6$Sn$_5$ alloy and Cu$_6$Sn$_5$/Sn composite were prepared via dealloying and their performance as lithium-ion battery anodes were tested. The dealloyed np-Cu$_6$Sn$_5$ presented an ultrafine ligament-channel structure with ligament size below 40 nm and BET specific area of 15.9 m$^2$ g$^{-1}$. The 3D nanoporous structure and high specific area endowed the anode with high lithium-ion battery performance. The anode displayed a capacity of higher than 600 mA h g$^{-1}$ for the initial five cycles at 0.1 A g$^{-1}$. It also had excellent cycling performance for at least 350 cycles at 0.1 A g$^{-1}$, with a reversible capacity of higher than 200 mA h g$^{-1}$. The ex situ XRD patterns reveal the reverse phase transformation between Cu$_6$Sn$_5$ and Li$_2$CuSn. Similar performance was obtained from Cu$_6$Sn$_5$/Sn composite. This study provided a practice for fabricating highly stable Sn-based anode in lithium-ion batteries.

**Institutional Review Board Statement:** Not applicable.

**Informed Consent Statement:** Not applicable.

**Data Availability Statement:** Not applicable.

**Conflicts of Interest:** The authors declare no conflict of interest.

## References

1. Liu, D.; Liu, Z.J.; Li, X.; Xie, W.; Wang, Q.; Liu, Q.; Fu, Y.; He, D. Group IVA element (Si, Ge, Sn)-based alloying/dealloying anodes as negative electrodes for full-cell lithium-ion batteries. *Small* **2017**, *13*, 1702000. [CrossRef]
2. Qiu, Z.; Zhang, Y.; Liu, Z.; Gao, Y.; Liu, J.; Zeng, Q. Stabilizing Ni-rich $LiNi_{0.92}Co_{0.06}Al_{0.02}O_2$ cathodes by boracic polyanion and tungsten cation Co-doping for high-energy lithium-ion batteries. *ChemElectroChem* **2020**, *7*, 3811–3817. [CrossRef]
3. Deng, K.; Zeng, Q.; Wang, D.; Liu, Z.; Wang, G.; Qiu, Z.; Zhang, Y.; Xiao, M.; Meng, Y. Nonflammable organic electrolytes for high-safety lithium-ion batteries. *Energy Storage Mater.* **2020**, *32*, 425–447. [CrossRef]
4. Zhang, C.; Xie, Z.; Yang, W.; Liang, Y.; Meng, D.; He, X.; Liang, P.; Zhang, Z. $NiCo_2O_4$/biomass-derived carbon composites as anode for high-performance lithium ion batteries. *J. Power Sources* **2020**, *451*, 227761. [CrossRef]
5. Shi, Y.; Song, M.; Zhang, Y.; Zhang, C.; Gao, H.; Niu, J.; Ma, W.; Qin, J.; Zhang, Z. A self-healing $CuGa_2$ anode for high-performance Li ion batteries. *J. Power Sources* **2019**, *437*, 226889. [CrossRef]
6. Ast, J.; Ghidelli, M.; Durst, K.; Göken, M.; Sebastiani, M.; Korsunsky, A. A review of experimental approaches to fracture toughness evaluation at the micro-scale. *Mater. Des.* **2019**, *173*, 107762. [CrossRef]
7. Wu, X.L.; Guo, Y.G.; Wan, L.J. Rational design of anode materials based on Group IVA elements (Si, Ge, and Sn) for lithium-ion batteries. *Chem. Asian J.* **2013**, *8*, 1948–1958. [CrossRef] [PubMed]
8. Bruce, P.G.; Scrosati, B.; Tarascon, J.M. Nanomaterials for rechargeable lithium batteries. *Angew. Chem. Int. Ed.* **2008**, *47*, 2930–2946. [CrossRef] [PubMed]
9. Yu, Y.; Gu, L.; Lang, X.; Zhu, C.; Fujita, T.; Chen, M.; Maier, J. Li storage in 3D nanoporous Au-supported nanocrystalline tin. *Adv. Mater.* **2011**, *23*, 2443–2447. [CrossRef] [PubMed]
10. Tarascon, J.M.; Armand, M. Issues and challenges facing rechargeable lithium batteries. *Nature* **2001**, *414*, 359–367. [CrossRef] [PubMed]
11. Liu, J.; Chen, X.; Kim, J.; Zheng, Q.; Ning, H.; Sun, P.; Huang, X.; Liu, J.; Niu, J.; Braun, P.V. High volumetric capacity three-dimensionally sphere-caged secondary battery anodes. *Nano Lett.* **2016**, *16*, 4501–4507. [CrossRef]
12. Xu, Y.; Zhu, Y.; Liu, Y.; Wang, C. Electrochemical performance of porous carbon/tin composite anodes for sodium-ion and lithium-ion batteries. *Adv. Energy Mater.* **2013**, *3*, 128–133. [CrossRef]
13. Datta, M.K.; Epur, R.; Saha, P.; Kadakia, K.; Park, S.K.; Kumta, P.N. Tin and graphite based nanocomposites: Potential anode for sodium ion batteries. *J. Power Sources* **2013**, *225*, 316–322. [CrossRef]
14. Luo, B.; Wang, B.; Liang, M.; Ning, J.; Li, X.; Zhi, L. Reduced graphene oxide-mediated growth of uniform tin-core/carbon-sheath coaxial nanocables with enhanced lithium ion storage properties. *Adv. Mater.* **2012**, *24*, 1405–1409. [CrossRef]
15. Huang, Y.; Wu, D.; Han, S.; Li, S.; Xiao, L.; Zhang, F.; Feng, X. Assembly of tin oxide/graphene nanosheets into 3D hierarchical frameworks for high-performance lithium storage. *ChemSusChem* **2013**, *6*, 1510–1515. [CrossRef]
16. Luo, B.; Wang, B.; Li, X.; Jia, Y.; Liang, M.; Zhi, L. Graphene-confined Sn nanosheets with enhanced lithium storage capability. *Adv. Mater.* **2012**, *24*, 3538–3543. [CrossRef]
17. Liu, J.; Wen, Y.; van Aken, P.A.; Maier, J.; Yu, Y. Facile synthesis of highly porous Ni-Sn intermetallic microcages with excellent electrochemical performance for lithium and sodium storage. *Nano Lett.* **2014**, *14*, 6387–6392. [CrossRef] [PubMed]
18. Wang, X.; Han, W.; Chen, J.; Graetz, J. Single-crystal intermetallic M−Sn (M = Fe, Cu, Co, Ni) nanospheres as negative electrodes for lithium-ion batteries. *ACS Appl. Mater. Interfaces* **2010**, *2*, 1548–1551. [CrossRef] [PubMed]
19. Wu, C.; Maier, J.; Yu, Y. Sn-based nanoparticles encapsulated in a porous 3D graphene network: Advanced anodes for high-rate and long life Li-ion batteries. *Adv. Funct. Mater.* **2015**, *25*, 3488–3496. [CrossRef]
20. Su, L.; Fu, J.; Zhang, P.; Wang, L.; Wang, Y.; Ren, M. Uniform core–shell $Cu_6Sn_5$@C nanospheres with controllable synthesis and excellent lithium storage performances. *RSC Adv.* **2017**, *7*, 28399–28406. [CrossRef]
21. Zhang, X.; Liu, L.; Liu, J.; Cheng, T.; Kong, A.; Qiao, Y.; Shan, Y. Ultrafine $Cu_6Sn_5$ nanoalloys supported on nitrogen and sulfur-doped carbons as robust electrode materials for oxygen reduction and Li-ion battery. *J. Alloys Compd.* **2020**, *824*, 153958. [CrossRef]
22. Xing, Y.; Wang, S.; Fang, B.; Feng, Y.; Zhang, S. Three-dimensional nanoporous $Cu_6Sn_5$/Cu composite from dealloying as anode for lithium ion batteries. *Microporous Mesoporous Mater.* **2018**, *261*, 237–243. [CrossRef]
23. Xiang, P.; Liu, W.; Chen, X.; Zhang, S.; Shi, S. Facile one-step preparation of 3D nanoporous $Cu/Cu_6Sn_5$ microparticles as anode material for lithium-ion batteries with superior lithium storage properties. *Metall. Mater. Trans. A* **2020**, *51*, 5965–5973. [CrossRef]
24. Tan, X.F.; McDonald, S.D.; Gu, Q.; Hu, Y.; Wang, L.; Matsumura, S.; Nishimura, T.; Nogita, K. Characterisation of lithium-ion battery anodes fabricated via in-situ $Cu_6Sn_5$ growth on a copper current collector. *J. Power Sources* **2019**, *415*, 50–61. [CrossRef]
25. Liu, X.; Zhang, R.; Yu, W.; Yang, Y.; Wang, Z.; Zhang, C.; Bando, Y.; Golberg, D.; Wang, X.; Ding, Y. Three-dimensional electrode with conductive Cu framework for stable and fast Li-ion storage. *Energy Storage Mater.* **2018**, *11*, 83–90. [CrossRef]
26. Yu, L.; Miao, C.; Nie, S.; Wen, M.; Wang, J.; Tan, Y.; Xiao, W. Feasible preparation of $Cu_6Sn_5$ alloy thin-film anode materials for lithium-ion batteries from waste printed circuit boards by electrodeposition. *Solid State Ionics* **2021**, *364*, 115625. [CrossRef]
27. Sarakonsri, T.; Apirattanawan, T.; Tungprasurt, S.; Tunkasiri, T. Solution route synthesis of dendrite $Cu_6Sn_5$ powders, anode material for lithium-ion batteries. *J. Mater. Sci.* **2006**, *41*, 4749–4754. [CrossRef]

28. Zhang, C.; Xie, Z.; He, X.; Liang, P.; Zeng, Q.; Zhang, Z. Fabrication and characterization of nanoporous Cu-Sn intermetallics via dealloying of ternary Mg-Cu-Sn alloys. *CrystEngComm* **2018**, *20*, 6900–6908. [CrossRef]

29. Tan, X.F.; McDonald, S.D.; Gu, Q.; Wang, L.; Matsumura, S.; Nogita, K. The effects of Ni on inhibiting the separation of Cu during the lithiation of $Cu_6Sn_5$ lithium-ion battery anodes. *J. Power Sources* **2019**, *440*, 227085. [CrossRef]

30. Fan, X.-Y.; Zhuang, Q.-C.; Wei, G.-Z.; Huang, L.; Dong, Q.-F.; Sun, S.-G. One-step electrodeposition synthesis and electrochemical properties of $Cu_6Sn_5$ alloy anodes for lithium-ion batteries. *J. Appl. Electrochem.* **2009**, *39*, 1323–1330. [CrossRef]

31. Chen, J.; Yang, L.; Fang, S.; Hirano, S.-i.; Tachibana, K. Three-dimensional core–shell $Cu@Cu_6Sn_5$ nanowires as the anode material for lithium ion batteries. *J. Power Sources* **2012**, *199*, 341–345. [CrossRef]

32. Feng, Y.; Zhang, S.; Xing, Y.; Liu, W. Preparation and characterization of nanoporous $Cu_6Sn_5/Cu$ composite by chemical dealloying of Al–Cu–Sn ternary alloy. *J. Mater. Sci.* **2012**, *47*, 5911–5917. [CrossRef]

33. Gao, H.; Ma, W.; Yang, W.; Wang, J.; Niu, J.; Luo, F.; Peng, Z.; Zhang, Z. Sodium storage mechanisms of bismuth in sodium ion batteries: An operando X-ray diffraction study. *J. Power Sources* **2018**, *379*, 1–9. [CrossRef]

34. Gao, H.; Niu, J.; Zhang, C.; Peng, Z.; Zhang, Z. A dealloying synthetic strategy for nanoporous bismuth-antimony anodes for sodium ion batteries. *ACS Nano* **2018**, *12*, 3568–3577. [CrossRef]

35. Song, T.; Yan, M.; Gao, Y.; Atrens, A.; Qian, M. Concurrence of de-alloying and re-alloying in a ternary $Al_{67}Cu_{18}Sn_{15}$ alloy and the fabrication of 3D nanoporous Cu–Sn composite structures. *RSC Adv.* **2015**, *5*, 9574–9580. [CrossRef]

36. Sing, K.S.W.; Everett, D.H.; Haul, R.A.W.; Moscou, L.; Pierotti, R.A.; Rouquerol, J.; Siemieniewska, T. Reporting physisorption data for gas/solid systems with special reference to the determination of surface area and porosity. *Pure Appl. Chem.* **1985**, *57*, 603–619. [CrossRef]

37. Ghidelli, M.; Sebastiani, M.; Collet, C.; Guillemet, R. Determination of the elastic moduli and residual stresses of freestanding Au-TiW bilayer thin films by nanoindentation. *Mater. Des.* **2016**, *106*, 436–445. [CrossRef]